Water Resources Research

RESEARCH ARTICLE
10.1029/2020WR027808

A New Fractal Approach to Account for Capillary and Adsorption Phenomena in the Water Retention and Transfer Properties of Unsaturated Soils

Filip Stanić[1,2], Pierre Delage[2], Ioulia Tchiguirinskaia[1], Pierre-Antoine Versini[1], Yu-Jun Cui[2], and Daniel Schertzer[1]

[1]École des Ponts ParisTech, HM&Co, Marne-la-Vallée, France, [2]École des Ponts ParisTech, Navier/CERMES Marne-la-Vallée, France

Abstract To describe the water retention and transfer properties of an unsaturated soil over the whole range of matric suction, it is necessary to account for both capillary and adsorption phenomena. Existing models combine well-known empirical functions for capillary water at lower suctions and more physically based ones for adsorptive water at higher suctions. To determine their full set of parameters, they however require different optimization procedures, among which those coming from capillary models are empirical. In this context, the main objective of this work is to develop a simple and robust physically based model of the water retention and transfer properties of unsaturated soils valid from saturation to oven dryness. To do so, new capillary-based water retention and hydraulic conductivity functions founded on the fractal approach have been derived from the pore size distribution, by means of the Young-Laplace law and Mualem's model. To describe adsorption phenomena, these functions are combined with those used in the Peters-Iden-Durner (PID) model, providing a model along the full range of suctions, with less parameters than the existing models. Our work also shows that some parameters are directly determined from the experimental grain size distribution data (the fractal dimension), or from the water retention data (air entry suction and residual water content), leaving only two parameters to be optimized. The model was successfully validated with respect to published experimental data from 10 different coarse, sandy, and clayey soils.

Key Points:
- Hydraulic properties of unsaturated soils along the full range of matric suctions depend on both capillary and adsorption mechanisms
- Due to empirical nature of existing hydraulic properties models, values of their parameters are determined through the optimization process
- A new robust fractal-based model proposed in this work requires less parameters, and some can be directly determined from experimental data

Supporting Information:
- Supporting Information S1

Correspondence to:
F. Stanić,
filip.stanic@enpc.fr

Citation:
Stanić, F., Delage, P., Tchiguirinskaia, I., Versini, P.-A., Cui, Y.-J., & Schertzer, D. (2020). A new fractal approach to account for capillary and adsorption phenomena in the water retention and transfer properties of unsaturated soils. *Water Resources Research*, *56*, e2020WR027808. https://doi.org/10.1029/2020WR027808

Received 28 APR 2020
Accepted 8 NOV 2020
Accepted article online 16 NOV 2020

1. Introduction

The most widely used water retention curves (WRCs) (e.g., Brooks & Corey, 1964; Fredlund & Xing, 1994, or Kosugi, 1996; van Genuchten, 1980) are semiempirical relations fitted from experimental data. As recalled in Leong and Rahardjo (1997), hydraulic conductivity functions have been derived from WRCs through statistical models (Hoffmann-Riem et al., 1997), among which Burdine's (1953) and Mualem's (1976) are the most widely used. These models consider unsaturated soils as a bunch of parallel capillary tubes of various diameters, with water saturation governed by the Young-Laplace capillary law that distinguishes, at a given suction, smaller water saturated tubes from larger unsaturated ones. Water flux through the saturated tubes is controlled by the Hagen-Poiseuille law. This empirical approach of WRCs has been completed by more physically based models based on the fractal theory (Ghanbarian-Alavijeh et al., 2011) and accounting for capillary effects within the pores of the partially saturated specimens (e.g., Bird et al., 2000; Russell & Buzzi, 2012). The pore-solid-fractal (PSF) model (Bird et al., 2000) is closely related to the grain size distribution (GSD) that is assumed to follow the same fractal law as the pore size distribution (PSD) (Perrier et al., 1999). Russell and Buzzi (2012) proposed a model based on two different fractal dimensions for pores and grains, respectively, that also accounts for the hysteresis of the WRCs. Hydraulic conductivity models have also been completed based on the fractal theory. Xu (2004) developed a hydraulic conductivity function based on the PSF approach, while Yang et al. (2014) extended a fractal-based hydraulic conductivity model to the hydraulic hysteresis of the WRC.

Capillary models assume water to be immobile at water contents lower than the residual one, which is not in agreement with some studies (Lenormand, 1990; Li & Wardlaw, 1986; Wang et al., 2013) that showed that the movement of the thin liquid films of water adsorbed along the clay particles cannot be neglected in clayey soils. The different mechanisms affecting the soil-water interaction in clayey soils can be found in

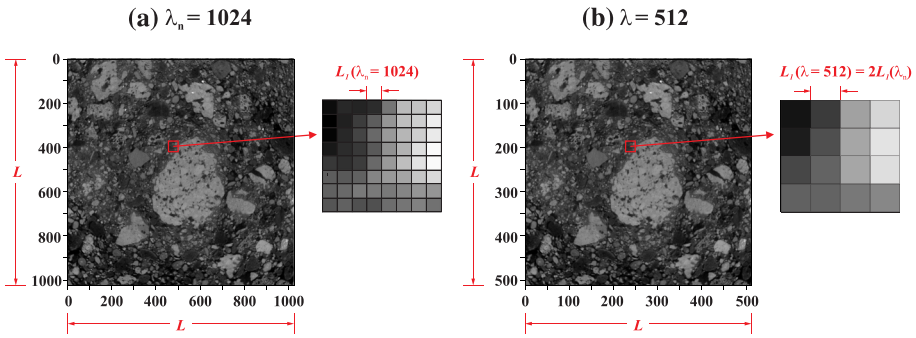

Figure 1. Upscaling of the renormalized ρ^{ind} field. Resolution λ of the field is decreased by factor 2, starting from $\lambda_n = 1{,}024$ (a) up to $\lambda = 512$ (b), while pixel size $L_1(\lambda)$ is increased by the same factor. Enlarged area of the image illustrates how pixels are grouped and their values are averaged as λ is reduced.

Lu and Zhang (2019) and Zhang and Lu (2019, 2020). Campbell and Shiozawa (1992) proposed a water retention function for the adsorbed water, that decreases linearly toward zero in a semi–log scale. Various hydraulic conductivity functions for the film flow were proposed by Tuller and Or (2001) and Tokunaga (2009), and various models accounting for both capillary and adsorbed phenomena along the whole range of suction between saturated and dry states have been developed. Peters (2013) used the water retention models of both van Genuchten (1980) and Kosugi (1996), in combination with Mualem's model for the capillary-dominated suction zone, completed by using Campbell and Shiozawa's (1992) and Tokunaga's (2009) functions in the high suction zone, where film-dominated flow occurs. To cope with mathematical discontinuity at the air-entry suction met in Campbell and Shiozawa's (1992) function, Iden and Durner (2014) proposed, in the so-called Peters-Iden-Durner (PID) model, a continuously differentiable function. This approach was upgraded by Rudiyanto et al. (2015) to account for hysteresis, while a mathematically continuous model based on Fredlund and Xing's (1994) function has been recently proposed by Wang et al. (2016). Also, Lu (2016) proposed a full suction range WRC model that uses a new equation for adsorptive water as a function of matric potential and a cavitation probability function for describing the transition between capillary and adsorption regimes.

All these models have shown rather good agreement with published data for a variety of soils along the full range of suction. However, optimization tools are necessary to properly fit experimental data, mostly because of the poor physical basis of the water retention functions in the capillary range. Fractal-based capillary models can be used as an alternative, but they suppose a fractal GSD, which is not in agreement with a recent study (Stanić, 2020) showing, in the case of grains of various densities, their multifractal nature.

In this work, a new fractal-based capillary model linked with the multifractal GSD function proposed by Stanić (2020) is combined with the PID model to account for the retention and transfer properties of both a sandy and a clayey soil, along the whole suction range. The performance of this model is tested by considering published data of 14 different soils.

2. Methodology

2.1. A New Fractal-Based Approach of the Pore Size Distribution

A new fractal-based PSD model is now presented, together with the derived hydraulic conductivity functions and the link with the multifractal-based GSD model. Figure 1 shows, at two consecutive resolutions, an example of a grayscale image of a coarse volcanic material investigated in Stanić et al. (2019). The image resolution, given on the edges of the square images, is defined by the ratio $\lambda = L/L_1(\lambda)$ between the size L (L) of the image and that ($L_1(\lambda)$) of a single pixel. In Figure 1, grains of various sizes and densities exhibit various gray levels (darker—lower densities and brighter—higher ones), while intergrains voids are in black. Gray levels are characterized by a dimensionless density indicator $\rho^{ind} \geq 0$ (see Stanić, 2020), where $\rho^{ind} = 0$ corresponds to pores full of air.

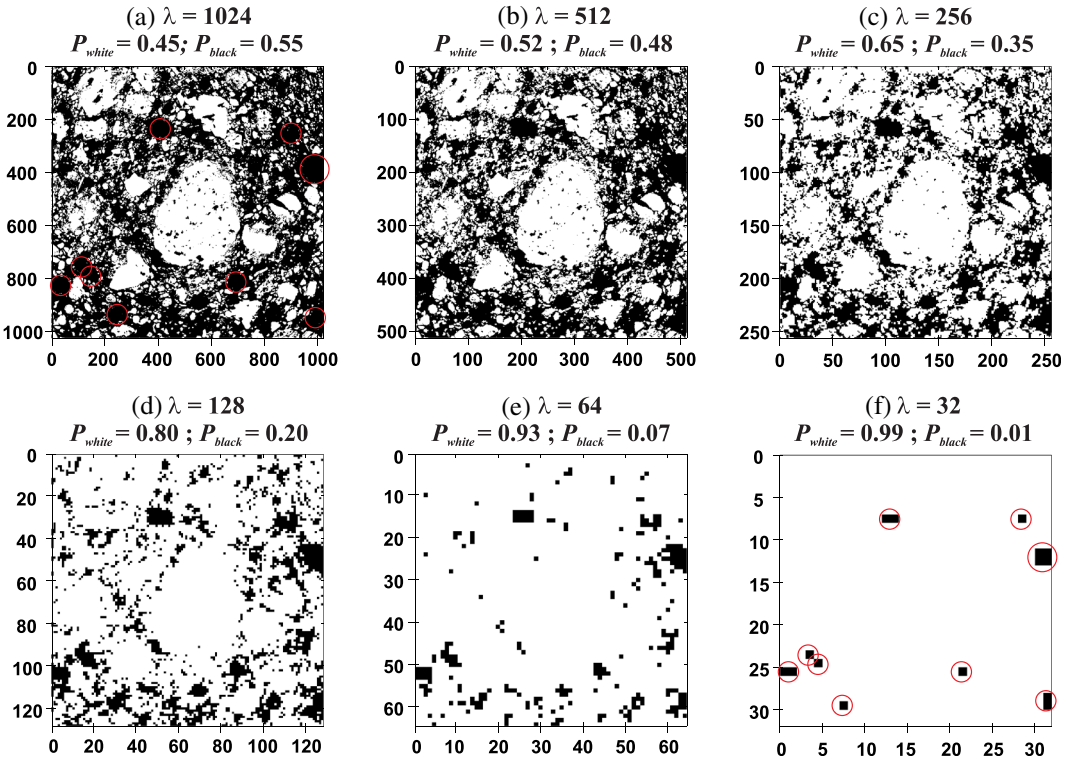

Figure 2. Procedure for determination of the fractal dimension of grains (white pixels). Resolution λ of the binary image decreases from $\lambda_n = 1{,}024$ to $\lambda_{min} = 32$.

Starting from the initial resolution $\lambda_n = 1{,}024$ (Figure 1a), one applies the standard upscaling procedure by reducing λ stepwise. By averaging groups of four neighbor pixels distributed in square, λ decreases by a factor $\sqrt{4} = 2$, while the pixel size $L_1(\lambda)$ increases by the same factor (see Figure 1b).

At sufficiently large λ_n, it is reasonable to assume that pores and grains of all sizes can be recognized from $\rho^{ind}(\lambda_n)$ field. This means that ρ^{ind} values at λ_n are either equal to or larger than $\rho^{ind}_{s,\,min}$, representing grains (see Appendix A), or equal to 0, then representing pores full of air (black areas). Intermediate ρ^{ind} values appear at lower resolutions ($\lambda < \lambda_n$) when averaging $\rho^{ind} \geq \rho^{ind}_{s,\,min}$ values with $\rho^{ind} = 0$ while upscaling.

As explained in Stanić (2020), by counting the values characterized by $\rho^{ind} \geq \rho^{ind}_{s,\,min}$ at each λ, it is possible to determine a cumulative representation of grains with sizes equal to or larger than the actual pixel size $L_1(\lambda)$. In order to determine the cumulative representation of pores ($\rho^{ind} = 0$), one can apply the standard Box-counting method (Feder, 1988; Yu & Cheng, 2002) on grain particles recognized at λ_n. To do so, all $\rho^{ind} \geq \rho^{ind}_{s,\,min}$ values (grains) at λ_n are first set to a constant value (e.g., 1), since the densities of grains are not of interest here, but only their spatial distribution. Thus, the gray-level image of Figure 1a is transformed into the binary black-white image of Figure 2a, where grains are represented in white ($\rho^{ind} = 1$) and pores in black color ($\rho^{ind} = 0$). The black-white image (Figure 2a) is then upscaled as explained above, where at each λ all ρ^{ind} values between 0 and 1 created by averaging, are reset to one (white), while clean $\rho^{ind} = 0$ (black) remain. Since black pixels ($\rho^{ind} = 0$) surrounded by at least one neighbor white pixel ($\rho^{ind} = 1$) turn into a twice as large white pixel after averaging, all the individual pores presented with a single black pixel vanish when λ is reduced. Hence, the presented box-counting method enables to determine a cumulative representation of pores (black areas) that are equal to or larger than the actual pixel size $L_1(\lambda)$.

Figure 2 shows that as λ decreases from 1,024 to 32, the pores (black pixels) smaller than the actual pixel size $L_1(\lambda)$ vanish, while those equal to or larger remain. Thus, solely the largest pores are recognized at λ_{min} (Figure 2f), while no black areas can be observed at $\lambda < \lambda_{min}$. Indeed, some of the largest black areas

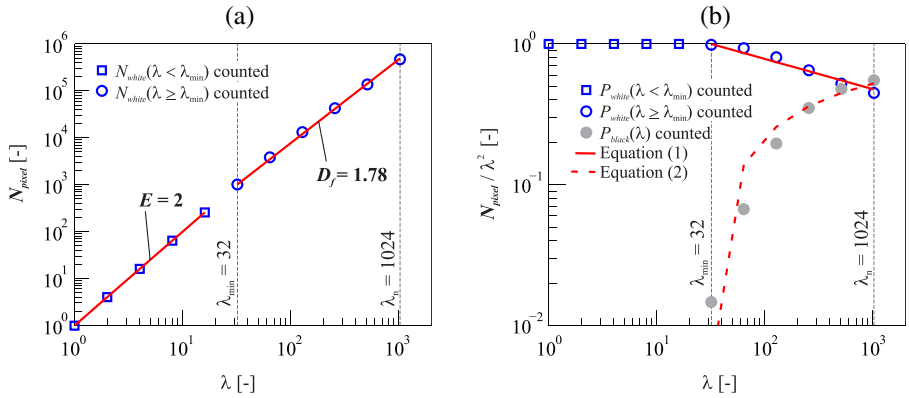

Figure 3. (a) Empty dots and squares illustrate the number of white pixels, counted at different λ of Figure 2, for $\lambda \geq \lambda_{min}$ and $\lambda < \lambda_{min}$, respectively; the slope of the $N_{white}(\lambda \geq \lambda_{min})$ corresponds to the value of D_f, while that of $N_{white}(\lambda < \lambda_{min})$ is equal to E. (b) Empty and filled dots illustrate the representations of white and black pixels for $\lambda \geq \lambda_{min}$, while solid and dashed lines illustrate the change of those pixels according to Equations 1 and 2, respectively.

recognized at $\lambda_n = 1{,}024$ are marked in Figure 2a and still observed in Figure 2f at $\lambda_{min} = 32$, while those smaller than $L_1(\lambda_{min})$ disappeared. This provides the link between the actual pore diameter d_p and $L_1(\lambda)$ ($d_p = L_1(\lambda)$), that is further used in the development of the fractal-based PSD model.

Since the box-counting method is applied on grain particles recognized at λ_n, the corresponding fractal dimension of grains can be determined from the slope of the best fitting linear regression that goes through the counted number of white pixels ($N_{white}(\lambda)$) plotted against λ in log-log scale. As illustrated in Figure 3a, the slope of the linear regression can be divided in two. For $\lambda < \lambda_{min}$ it is equal to the Euclidean dimension ($E = 2$ or 3 for two- or three-dimensional space, respectively), since only white pixels occur at this range, while for $\lambda \geq \lambda_{min}$ it is equal to $D_f < E$. Since pores can be observed only at $\lambda \geq \lambda_{min}$, solely this range is considered in this study. If results presented in Figure 3a are expressed in the form of representations ($P_{white}(\lambda) = \frac{N_{white}(\lambda)}{\lambda^E}$, where $E = 2$), the slope of the linear regression becomes equal to ($D_f - E$) for $\lambda \geq \lambda_{min}$ (see Figure 3b). Therefore, $P_{white}(\lambda \geq \lambda_{min})$ can be expressed using a power (fractal) law:

$$P_{white}(\lambda) = \left(\frac{\lambda}{\lambda_{min}}\right)^{D_f - E} \tag{1}$$

Black pixels representing pores (filled dots in Figure 3) are complementary to white ones ($P_{black}(\lambda) = P_{pores}(\lambda) = 1 - P_{white}(\lambda)$), resulting in the following expression:

$$P_{pores}(\lambda) = 1 - \left(\frac{\lambda}{\lambda_{min}}\right)^{D_f - E} \tag{2}$$

Given that $L_1(\lambda) = d_p$, the ratio $\frac{\lambda}{\lambda_{min}} = \frac{L/d_p}{L/d_{p,\,max}}$ is equal to $\frac{d_{p,\,max}}{d_p}$, where $d_{p,max}$ is the maximal pore diameter (L) related to λ_{min}. Thus, Equation 2 describes the representation of pores with diameter equal to or larger than d_p.

In order to transform the representation function into a cumulative distribution function describing the probability of exceeding d_p, Equation 2 needs to be renormalized with respect to the initial representation of pores met at λ_n, which is, according to Equation 2, equal to $P_{pores}(\lambda_n) = 1 - \left(\frac{\lambda_n}{\lambda_{min}}\right)^{D_f - E}$. Since $\frac{\lambda_n}{\lambda_{min}} = \frac{d_{p,\,max}}{d_{p,\,min}}$, where $d_{p,min}$ is the minimal pore diameter (L) related to λ_n, the probability of exceeding d_p is as follows:

$$P(d \geq d_p) = \frac{1 - \left(\frac{d_{p,\,max}}{d_p}\right)^{D_f - E}}{1 - \left(\frac{d_{p,\,max}}{d_{p,\,min}}\right)^{D_f - E}} \tag{3}$$

At sufficiently high λ_n, it can be assumed that $P_{pores}(\lambda_n)$ is equal to the experimentally determined porosity φ. Hence, the PSD expressing the cumulative distribution of pores smaller than d_p can finally be written as follows:

$$P(d < d_p) = 1 - \frac{1 - \left(\frac{d_{p,\,max}}{d_p}\right)^{D_f - 3}}{\varphi} \tag{4}$$

where $\varphi = 1 - \left(d_{p,\,max}/d_{p,\,min}\right)^{D_f - 3}$ and $E = 3$, since the PSD is based on the representation of pore volumes.

Stanić (2020) showed that, in order to describe the GSD curve, it is necessary to use different fractal dimensions for grains larger than different referenced grain diameters d_g (multifractal formalism). In this work, however, a single fractal dimension D_f, related to grains equal to or larger than the minimal grain diameter $d_{g,min} = L_1(\lambda_n)$, is used for describing the PSD (Equation 4). This way, the link between the PSD and the GSD is preserved, enabling the determination of D_f from the GSD model (see Appendix A). Since D_f is related to grains, the boundary value $D_f = E = 3$ describes the space covered only with grains without pores, leading to a zero porosity ($\varphi = 1 - (d_{p,max}/d_{p,min})^0 = 0$).

In the case of well-graded materials, smaller grains fill the voids between larger ones, creating pores of different sizes. This causes the black areas in the black-white soil image to resist longer to the upscaling procedure, securing less steep linear regression of white pixels (see Figure 3) and hence higher D_f. On the contrary, grains of uniform size create narrow spectrum of pore sizes that vanish rather rapidly once the upscaling procedure is started. This results in a steeper slope of the linear regression and hence lower D_f. Finally, it can be concluded that a lower D_f is related to poorly graded materials like clean sands with a narrow range of grain sizes, while higher D_f (closer to E) is related to well-graded materials.

2.2. Water Retention

When accounting for the water content change along the drying path of the WRC from saturation to oven dryness, both capillary and adsorptive water need to be considered. In this case, the total water content $\theta^{tot}(h_k)$ can be written, as proposed by Iden and Durner (2014):

$$\theta^{tot}(h_k) = (\theta_s - \theta_r) S_e^{cap}(h_k) + \theta_r S_e^{ads}(h_k) \tag{5}$$

where $S_e{}^{cap}(h_k)$ and $S_e{}^{ads}(h_k)$ are the relative saturations [0–1] of capillary and adsorptive water, respectively, θ_s and θ_r are the saturated and residual water contents (−), respectively, and h_k is the suction expressed in terms of water height (pressure head) (L). Equation 5 indicates that capillary water is dominant at lower h_k ($\theta_s < \theta < \theta_r$), while for significantly higher h_k values ($\theta < \theta_r$), the adsorptive water mainly remains.

To date, semiempirical water retention functions (Brooks & Corey, 1964; Fredlund & Xing, 1994; Kosugi, 1996; van Genuchten, 1980, etc.) are most often used to account for water retention effects in the capillary range, with no consideration of the residual adsorbed water at high suction. In this study, a new physically based function based on Equation 4 and the Young-Laplace law is proposed in the capillary range. Following the Young-Laplace law, once suction h_k is imposed to an initially saturated porous medium, all pores with diameters smaller than $d_p = C/h_k$ m ($C \approx 2.8 \times 10^{-5}$ expresses the Young-Laplace law and is a function of water/solid interaction properties) are emptied. Thus, $S_e{}^{cap}(h_k)$ can be simply obtained from Equation 4:

$$S_e^{cap}(h_k) = \frac{\theta^{cap}(h_k) - \theta_r}{\theta_s - \theta_r} = \begin{cases} 1, & h_k < h_{k,\,a} \\ 1 - \dfrac{1 - \left(\dfrac{h_k}{h_{k,\,a}}\right)^{D_f - 3}}{\theta_s - \theta_r}, & h_{k,\,a} \leq h_k \leq h_{k,\,r} \end{cases} \tag{6}$$

where $h_{k,a}$ is the air entry value suction (L), a maximal h_k corresponding to full saturation.

The suction $h_{k,r}$ corresponding to the extraction of all capillary water and to $\theta = \theta_r$ is obtained by writing $\left(S_e^{cap}\left(h_{k,r}\right) = 0\right)$, giving $h_{k,r} = h_{k,a}[1 - (\theta_s - \theta_r)]^{\frac{1}{D_f - 3}}$.

Thus, both $S_e{}^{cap}$ and $S_e{}^{ads}$ condition the value of θ^{tot} for $h_{k,a} \le h_k < h_{k,r}$, while only $S_e{}^{ads}$ remains for $h_k \ge h_{k,r}$ (see Equation 5). Note that Equation 6 does not account for the total porosity?, but for its part $(\theta_s - \theta_r)$ full of capillary water. This implies that Equation 6 is not differentiable for $h_k = h_{k,a}$ and $h_k = h_{k,r}$, unlike standard water retention functions. But it provides a better insight into the impact of the PSD on the retention properties, as pointed out in section 3, later on.

Based on the fact that adsorptive water linearly decreases toward zero in semi–log scale (Campbell & Shiozawa, 1992), Peters (2013) proposed an equation describing $S_e{}^{ads}$, that has been later replaced with a smoothed piecewise linear function proposed by Iden and Durner (2014), as follows:

$$S_e^{ads}(h_k) = \frac{\theta^{ads}(h_k)}{\theta_r} = 1 + \left(\log_{10}\left(\frac{h_{k,a}}{h_0}\right)\right)^{-1}\left\{\log_{10}\left(\frac{h_k}{h_{k,a}}\right) + b\ln\left[1 + e^{\log_{10}\left(\frac{h_{k,a}}{h_k}\right)/b}\right]\right\} \tag{7}$$

where b is a smoothing parameter that impacts $S_e^{ads}(h_k)$ near $h_k = h_{k,a}$ (see Iden & Durner, 2014, for more details) and h_0 is the suction (L) value (about 10^5 m) related to totally dry conditions $\theta^{tot}(h_0) = 0$. Even though Lu and Khorshidi (2015) reported some variation in h_0 for clay soils, a fixed value of $h_0 = 6.3 \times 10^4$ m has been adopted in this work, as suggested by Peters (2013), to reduce the number of model parameters. The higher the value of b, the smoother the $S_e^{ads}(h_k)$ function, with however the limitation that b should take a value between 0.1 and 0.3, as proposed by Iden and Durner (2014) based on a sensitivity analysis. They also proposed empirical expressions for determining b as function of the parameters of van Genuchten (1980)'s or Kosugi (1996)'s equations. Since Equation 6 is not differentiable for $h_k = h_{k,a}$, Equation 5 cannot be mathematically continuous regardless of the value of b. However, Equation 7, with a maximum value of $b = 0.3$, has been finally adopted to smooth θ^{tot} as much as possible in the zone around $h_k = h_{k,a}$, allowing better interpretation of measured data. Note that Equation 5 can be reduced to solely capillary model ($\theta^{tot} = \theta^{cap}$) if water is considered to be immobile for $\theta < \theta_r$ ($\theta^{ads} = \theta_r$ for every h_k).

2.3. Hydraulic Conductivity

According to Peters (2013), the hydraulic conductivity K^{tot} along the whole suction range can be presented as the sum of two components K^{cap} and K^{film}, if the isothermal vapor conductivity is neglected:

$$K^{tot} = K^{cap} + K^{film} = K_s{}^{cap}K_r{}^{cap} + K_s{}^{film}K_r{}^{film}, \tag{8}$$

where $K_s{}^{cap}$ and $K_s{}^{film}$ are the saturated hydraulic conductivities (L/T) for capillary and adsorptive (film) water, respectively, while $K_r{}^{cap}$ and $K_r{}^{film}$ are the corresponding relative hydraulic conductivity functions (−), respectively. Note that K^{film} is several orders of magnitude lower than K^{cap} and thus has a negligible influence on K^{tot} for $\theta > \theta_r$. If the film flow is ignored ($K^{film} = 0$), Equation 8 is reduced to a capillary hydraulic conductivity function.

As previously explained, the bulk hydraulic conductivity can be calculated by integrating the contributions of water fluxes through the saturated capillary tubes of different sizes that correspond to the actual water content or saturation degree. Based on the assumption that the water movement through straight capillary tubes follows Hagen-Poiseuille's law and that exponent l can account for the tortuosity effect, a general analytical form of the relative hydraulic conductivity of capillary water has been given by Hoffmann-Riem et al. (1997) as follows:

$$K_r{}^{cap}\left(S_e^{cap}\right) = \left(S_e^{cap}\right)^l\left(\frac{\int_0^{S_e^{cap}} h_k{}^{-k}\,dS_e^{cap}}{\int_0^1 h_k{}^{-k}\,dS_e^{cap}}\right)^{\beta} \tag{9}$$

where parameters l, k, and β vary for different models. The commonly used Mualem (1976) model can be obtained for $k = 1$ and $\beta = 2$, while l remains a fitting parameter, as proposed by many authors (Neto et al., 2011; Peters et al., 2011; Schaap & Leij, 1999; Yates et al., 1991, among others). In this case, it is

more convenient to integrate Equation 9 with respect to h_k, which can be done by introducing the derivative of Equation 6 $\left(dS_e^{cap} = \frac{D_f - 3}{h_{k,a}(\theta_s - \theta_r)}\left(\frac{h_k}{h_{k,a}}\right)^{D_f - 4} dh_k\right)$ and by changing the boundaries of the integration with respect to the boundaries in Equation 6:

$$K_r{}^{cap}(h_k) = \left(S_e^{cap}\right)^l \left(\frac{\int_{h_{k,r}}^{h_k} h_k{}^{D_f - 5} dh_k}{\int_{h_{k,r}}^{h_{k,a}} h_k{}^{D_f - 5} dh_k}\right)^2 \tag{10}$$

Finally, $K_r{}^{cap}(h_k)$ can be rewritten as follows:

$$K_r{}^{cap}(h_k) = \begin{cases} 1, & h_k < h_{k,a} \\ \left(1 - \frac{1 - \left(\frac{h_k}{h_{k,a}}\right)^{D_f - 3}}{\theta_s - \theta_r}\right)^l \left(\frac{\left(\frac{h_k}{h_{k,a}}\right)^{D_f - 4} - \left(\frac{h_{k,r}}{h_{k,a}}\right)^{D_f - 4}}{1 - \left(\frac{h_{k,r}}{h_{k,a}}\right)^{D_f - 4}}\right)^2, & h_{k,a} \le h_k \le h_{k,r} \end{cases} \tag{11}$$

where the values of the expression in the second brackets is included between 0 and 1, null for $h_k = h_{k,r}$ and equal to 1 for $h_k = h_{k,a}$.

Tokunaga (2009) showed that the hydraulic conductivity of the film decreases almost linearly with increasing suction in log-log scale, with a slope $a = -1.5$. Based on that, Peters (2013) proposed a simple function describing the film flow:

$$K_r{}^{film}\left(S_e^{ads}\right) = \left(\frac{h_0}{h_{k,a}}\right)^{-1.5\left(1 - S_e^{ads}\right)} \tag{12}$$

Besides Peters (2013), Zhang (2011) also proposed an analytical function that depends on many physical constants and hence brings additional uncertainties into the calculation. This is why this function was not adopted in this work. Note that parameter a can deviate from −1.5 (Equation 12), especially in case of clays, since this value was derived from the case of smooth spherical grains. Some authors, like Rudiyanto et al. (2015), included parameter a into the optimization process. In this work, $a = -1.5$ was adopted, like in Peters (2013) and Wang et al. (2016).

3. Results

The proposed model was validated with literature data for 14 different soils (sands, loams, and clays), presented in Table 1, that also provide for each soil the values of the five physically based model parameters (θ_r, $h_{k,a}$, D_f, K_s^{film}, and l), together with the squared correlation coefficient (R^2) used to rate the agreement between model and measurements. Among them, the Green Wave coarse granular material (Stanić et al., 2019) has a particular status. Indeed, it does not present any significant adsorption effect, but it is the only material for which the complete set of parameters needed is available, including the GSD curve that has not been provided for the other soils.

Figure 4 shows, for the Green Wave substrate, the GSD (a), the water retention (b—top graph), and the hydraulic conductivity function (b—bottom graph).

The other soils, for which only the hydraulic properties data were available, are divided into three groups. Figure 5 compares, for seven soils, the modeled water retention, and hydraulic conductivity function with experimental data. The same is presented in Figure 6 for three soils where the measured hydraulic conductivity was related to changes in water content, while in Figure 7 are compared simulated and measured WRCs for three different clay soils. Different soils in Figures 5–7 are arranged to respect the ascending order of D_f value in each figure.

In Figure 4–7, computed θ^{tot} values (Equation 5) are compared with measured water retention data. On the same figures, the calculated values of θ^{cap} (dashed line—Equation 6) and θ^{ads} (dash-dotted line —Equation 7) are also presented. Similarly, computed K^{tot} values (Equation 8) are compared with measured hydraulic conductivity data (Figure 4–6), together with the individual contributions of K^{cap} and K^{film} calculated by using Equations 11 and 12, respectively.

Table 1
Measured (θ_s, K_s^{cap}) and Determined/Adjusted Values (Highlighted in Gray) of the Model Parameters

Soil	Reference	θ_s (−)	K_s^{cap} (m/s)	D_f(−)	$h_{k,a}$ (m)	θ_r(−)	K_s^{film} (m/s)	l (−)	R^2 WRC	R^2 HCF
Shonai sand	Mehta et al. (1994)[a]	0.431	1.09E−04	2.680	0.12	0.064	1.74E−09	1.10	0.98	0.80
Wyoming bentonite	Likos and Lu (2003)[b]	0.700	—	2.680	50.00	0.332	—	—	0.99	—
Rehovot sand	Mualem (1976)[a]	0.400	1.27E−04	2.725	0.12	0.021	5.21E−10	0.30	0.99	0.99
Gilat loam	Mualem (1976)[a]	0.440	2.00E−06	2.790	0.33	0.168	5.21E−09	1.00	0.99	0.97
Pachappa loam	Jackson et al. (1965)[a]	0.460	2.00E−06	2.860	0.50	0.138	9.26E−09	1.20	0.99	0.98
Pachappa fine sandy clay	Mualem (1976)[a]	0.330	1.40E−06	2.873	0.50	0.111	2.31E−09	0.20	0.99	0.98
Adelanto loam	Jackson et al. (1965)[a]	0.430	4.50E−07	2.905	1.50	0.261	2.89E−09	0.30	0.99	1.00
Georgia kaolinite	Likos and Lu (2003)[b]	0.570	—	2.905	1.60	0.118	—	—	0.99	—
Sandy loam	Pachepsky et al. (1984)[a]	0.425	9.00E−07	2.930	0.18	0.091	9.26E−09	−0.50	0.99	0.96
GW substrate	Stanić et al. (2019)	0.395	8.11E−06	2.950	0.009	0.045	1.16E−08	−1.35	0.99	1.00
Okcheon 2	Oh et al. (2015)[c]	0.435	2.38E−06	2.960	0.45	0.200	1.16E−08	−1.35	0.99	0.99
Seochang	Oh et al. (2015)[c]	0.379	9.13E−07	2.965	0.18	0.050	1.39E−08	−1.30	0.96	0.99
Clay loam	Pachepsky et al. (1984)[d]	0.500	2.90E−07	2.970	0.40	0.337	1.39E−08	1.00	0.99	0.99
Arizona-18	Jensen et al. (2014)	0.429	—	2.982	2.00	0.361	—	—	1.00	—

[a]Taken from Rudiyanto et al. (2015). [b]Taken from Lu (2016). [c]θ_s is calculated based on the void ratio e (−) as $\theta_s = \varphi = \frac{1}{1+e}$. [d]Taken from Zhang (2011), where the measured θ_s and K_s^{cap} values are not provided and hence roughly estimated from the experimental water retention and hydraulic conductivity data.

4. Discussion

Figure 4–6 show that, unsurprisingly, K^{film} has a negligible effect on K^{tot} in the lower range of suctions ($h_k < h_{k,r}$), since K_s^{film} is several orders of magnitude lower than K_s^{cap}. For $h_k \geq h_{k,r}$, θ^{cap} becomes constant and equal to θ_r, resulting in having θ^{tot} only controlled by θ^{ads}, with no effect of K^{cap} on K^{tot} ($K^{tot} = K^{film}$).

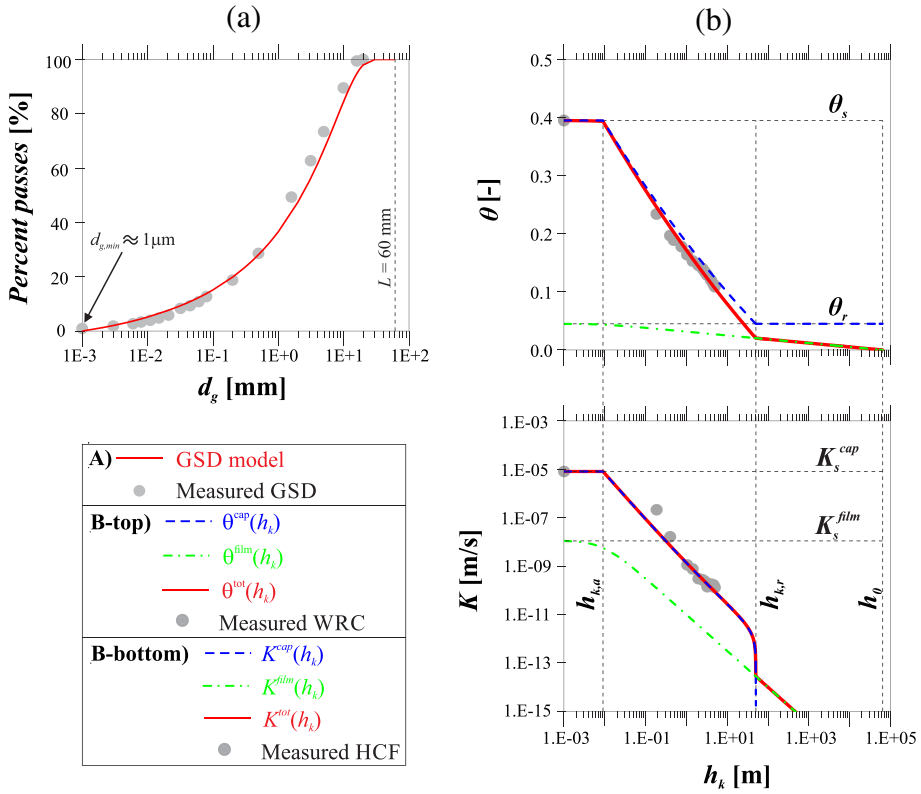

Figure 4. (a) Comparison between the measured GSD (filled dots) and the multifractal based GSD model (after Stanić, 2020); (b) Comparison between the proposed model and the water retention (top graph) and hydraulic conductivity (bottom graph) experimental data taken from Stanić et al. (2019).

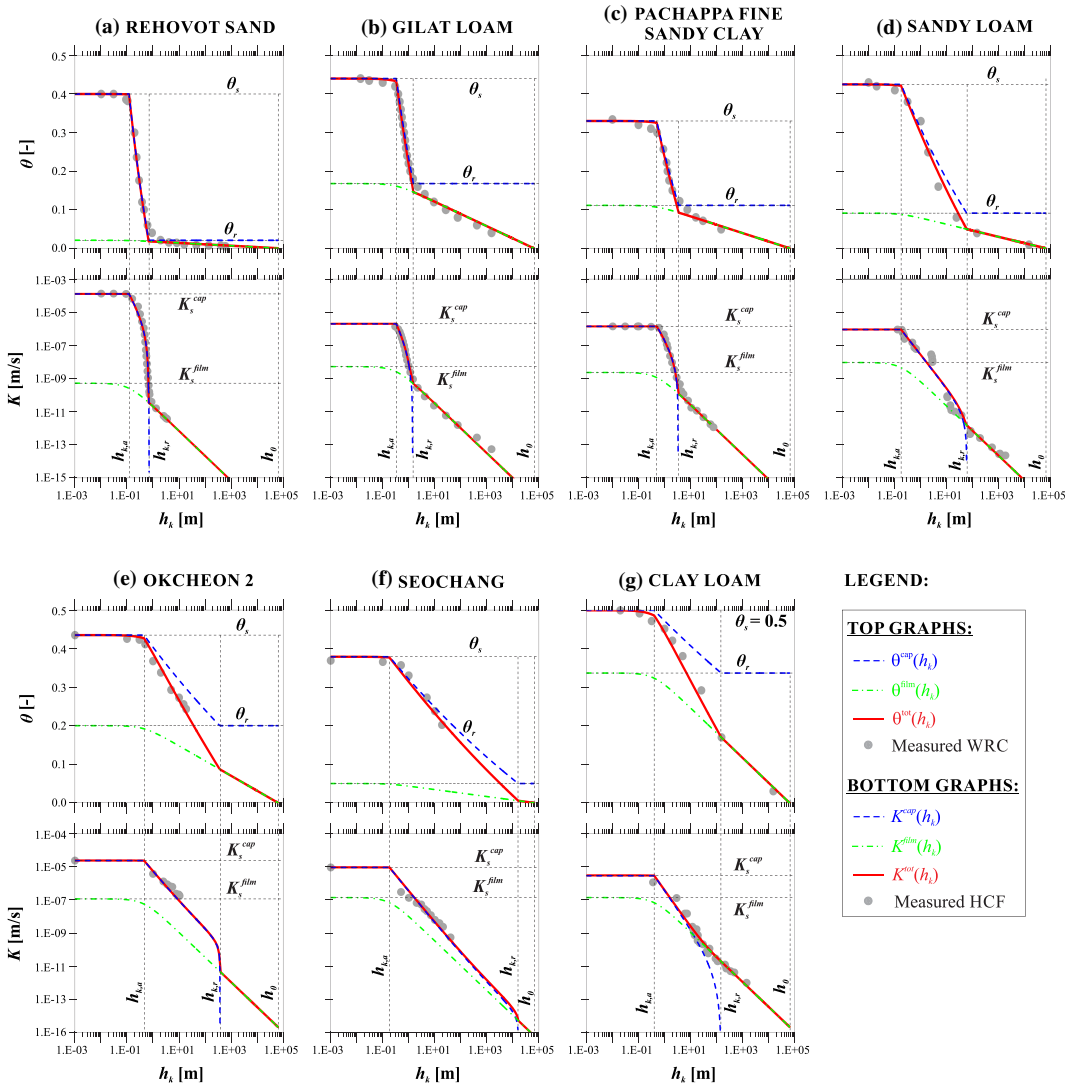

Figure 5. Comparison between the proposed model and seven data sets from the literature. Top graphs present water retention data, and bottom graphs hydraulic conductivity functions, all with respect to suction changes.

The data of the Green Wave substrate (Figure 4) show the relation between the material GSD and its hydraulic properties in unsaturated state. As explained in the Appendix A, based on the GSD model parameters (taken from Stanić, 2020, with $L = 60$ mm, $d_{g,min} \approx 1$ μm, $\rho^{ind}_{s,min} = \rho_{s,min}/\rho_{bulk} = 1.5$, $C_1 = 2.25 \times 10^{-2}$ and $\alpha = 1.6$) and a value of $d_{p,max}$, it is possible to determine D_f using Equation A4. Since the value of $d_{p,max}$ is unknown in case of the Green Wave substrate, value of $h_{k,a}$ can be used instead by knowing that these two parameters are reversely proportional according to the Young-Laplace law ($d_{p,max} \approx 2.8 \times 10^{-5}/h_{k,a}$ m). Therefore, four parameter values (θ_r, $h_{k,a}$, K_s^{film}, and l) are adjusted and $D_f = 2.95$ is computed based on the GSD parameters and $h_{k,a} = 9 \times 10^{-3}$ m, in order to provide the best interpretation of the water retention and transfer properties in Figure 4b. The possibility to determine D_f from GSD data confirms the relevance of our physically based model, that does not need using any optimization tools, as most other ones.

For the other soils, the GSD curves were not available, and hence, D_f was manually adjusted based on water retention data. The value of $h_{k,a}$ can be easily estimated from water retention data, since the water content for $h_k < h_{k,a}$ remains almost constant, while for $h_k > h_{k,a}$ it starts to decrease more significantly depending on the value of D_f (see Equation 6). Also, the value of θ_r can be computed from Equation 6 by estimating the residual $h_{k,r}$, after which water content starts to decrease less significantly ($S_e^{cap}(h_{k,r}) = 0$):

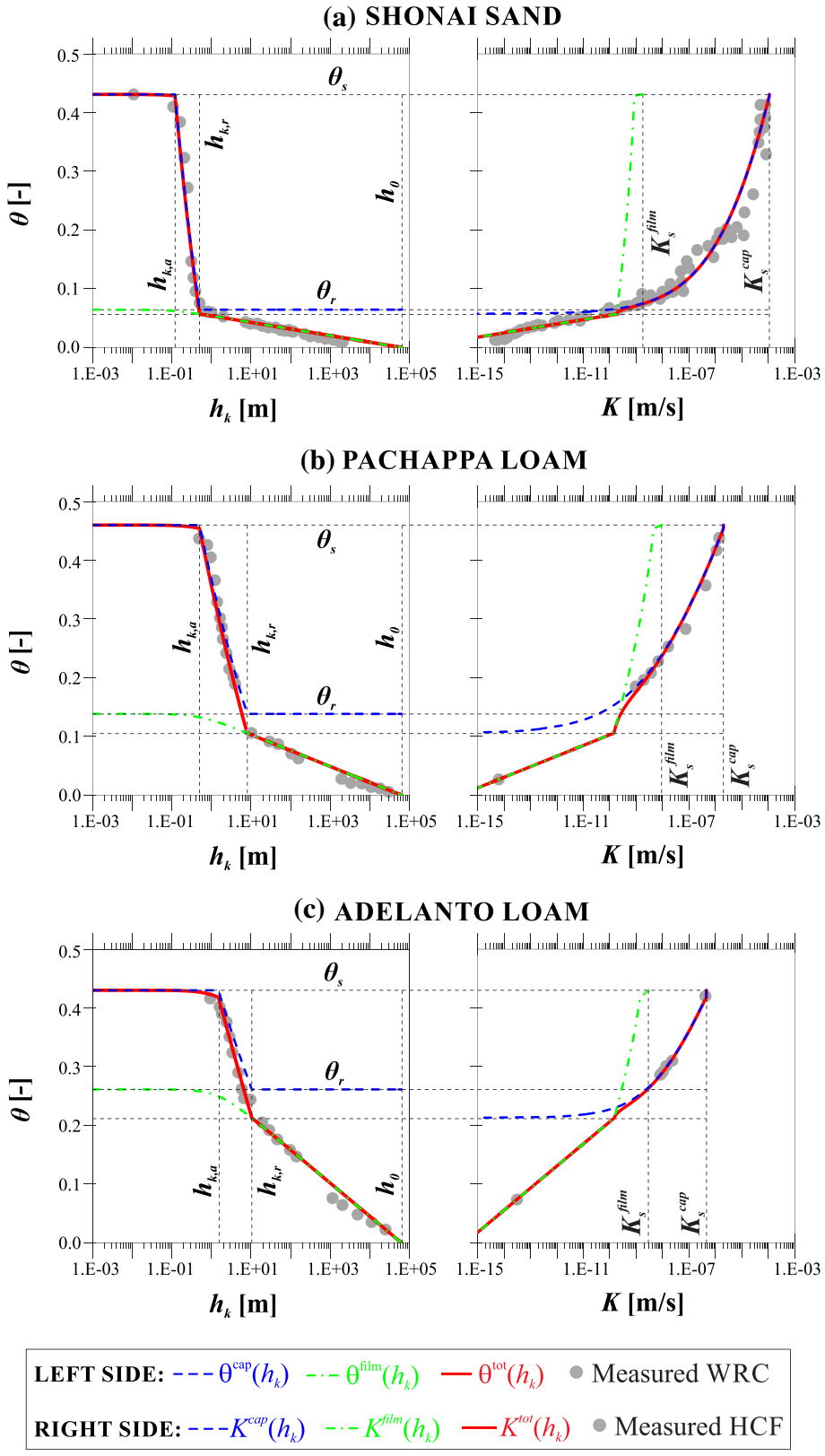

Figure 6. Comparison between the proposed model and three additional data sets from the literature. Left-side graphs deal with water retention data, whereas right-side graphs deal with hydraulic conductivity functions with respect to changes in water content.

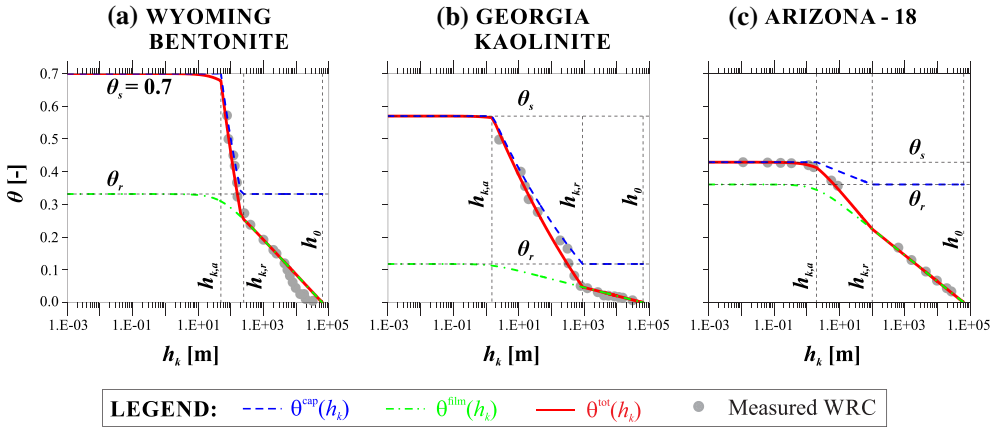

Figure 7. Comparison between the proposed model and the published experimental water retention data for three clayey soils.

$$\theta_r = \theta_s - 1 + \left(\frac{h_{k,\,r}}{h_{k,\,a}}\right)^{D_f\,-\,3}. \tag{13}$$

Finally, K_s^{film} and l were adjusted based on the agreement between Equation 8 and the experimental hydraulic conductivity data. Parameter l affects the regression of K^{cap} together with D_f, in such a way that smaller values of l (including negative values) ensure less significant decrease of K^{cap} with suction increase, and vice versa. Also, the value of K_s^{film} only moves the K^{film} curve upward or downward, without affecting its regression (Equation 12). The values of l and K_s^{film} cannot be predefined or determined based on the WRC, which means that the hydraulic conductivity function cannot be reliably predicted without measurements, as already observed for any analytical hydraulic conductivity function.

Unsurprisingly, the WRCs appear to be steeper in the case of sands (Figures 5a and 6a), which corresponds to lower D_f values and indicates that the sands tested are poorly graded, with a narrow range of pore sizes. This results in having the most significant change in water content and hydraulic conductivity over the smallest ratio of suctions ($h_{k,r}/h_{k,a}$). A lower ratio ($h_{k,r}/h_{k,a}$) in combination to a lower D_f value results in a lower θ_r (see Equation 13). This is characteristic of sands with a small percentage of fine particles and no adsorption properties, as confirmed by the results of Figures 5a and 6a, where θ^{tot} is almost equal to θ^{cap} for $h_k < h_{k,r}$. In this case, it is possible to totally separate capillary and adsorptive mechanisms, without affecting the parameter values. Thus, $\theta^{tot} = \theta^{cap}$ for $h_k < h_{k,\mathrm{r}}$ and $\theta^{tot} = \theta^{ads}$ for $h_k \geq h_{k,\mathrm{r}}$. Moreover, the difference between K_s^{cap} and K_s^{film} is the most significant for these two soils (around 5 orders of magnitude).

Compared to sands, higher values of D_f are used to describe the hydraulic properties of loamy and clayey soils (Figures 5b–5d, 5g, 6b, and 6c). Larger θ_r values evidence the influence of adsorptive water. In the cases of sandy loam (Figure 5d), Adelanto loam (Figure 6c), and clay loam (Figure 5g) which contains 34% of clay particles, θ^{cap} clearly deviates from θ^{tot}, even at lower suctions, which is directly related to the higher values of θ_r and D_f. This means that a water retention function accounting solely for capillarity ($\theta^{tot} = \theta^{cap}$) is not satisfactory. In this case, a smaller D_f value is necessary to obtain good agreement between θ^{cap} and the water retention data. Furthermore, the difference between K_s^{cap} and K_s^{film} is about 2 orders of magnitude (even less for the clay loam), which is significantly lower compared to sands, confirming the stronger impact of adsorption mechanism. As commented before, high values of D_f are also related to well-graded granular materials with 5% to 15% of fine particles (<75 μm), presented in Figures 4, 5e, and 5f. Again, significant deviation between θ^{ads} and θ^{tot} at low suctions is related to the combination of high D_f and θ_r values, as it is the case of Okcheon 2 and Seochang soils (Figures 5e and 5f, respectively). Also, the Green Wave substrate, Okcheon 2, and Seochang soils show less significant decrease in hydraulic conductivity with respect to suction increase, which is described by negative l values (see Equation 10). The values of l have been adjusted by respecting the criterion that K^{cap} needs to be a decreasing and concave function (Peters et al., 2011).

Note that no measurements at high suctions were available for these three materials, so the parameters calibration was done based on the available data range.

To validate the proposed model over the adsorption-dominant suction range, it has been tested on the data of three different clay soils investigated by Lu (2016), including water retention data at high suctions (see Figure 7). According to the Unified Soil Classification System (USCS), the Wyoming bentonite (Figure 7a) and the Georgia kaolinite (Figure 7b) are classified as high and low plasticity clays (CH and CL), respectively. Both contain more than 98% of fines (see Likos & Lu, 2003, for more details), while the Arizona soil-18 (Figure 7c) contains about 50% of clay and 40% of silt particles (see Jensen et al., 2014). These three clayey soils show different behaviors in terms of water retention properties, and all are well described with the proposed model. Values of D_f vary from 2.68 in case of Wyoming bentonite, where a significant change in θ occurs over a small ($h_{k,r}/h_{k,a}$) ratio, to 2.982 in case of Arizona soil-18 with a slight slope of the WRC between $h_{k,a}$ and $h_{k,r}$. More significant deviation between the model and measurements can be found in the case of the Wyoming bentonite for $h_k > 10^3$ m. This is mostly due to the possible variation of the maximal suction h_0 in clay soils (see Lu & Khorshidi, 2015).

Most of the data presented here have been compared with different published models (Iden & Durner, 2014; Lu, 2016; Peters, 2013; Rudiyanto et al., 2015; Wang et al., 2016), with satisfactory agreements. However, usually more than five parameters, including some empirical ones, have to be considered in the optimization process for both the WRC and the HCF. In our model, two out of five parameters (D_f and θ_r) can be derived from soil properties. The determination of the three remaining parameters can then be achieved manually in a rather simpler way, due to their strong physical basis.

5. Conclusion

The main objective of this work was to develop a simple and robust physically based model of the water retention and transfer properties of unsaturated soils over the entire range of matric suctions, including both capillary and adsorption effects. This was done by introducing new capillary-based water retention and hydraulic conductivity functions based on a fractal approach, and by adopting the PID model to account for adsorption effects. Compared to available models, these functions, that depend on a smaller number of physically based parameters, are less empirical and ensure simple computations of their values by manual adjustment.

It has recently been shown (Stanić, 2020) that the GSD of material with various grain densities can be described by using a continual set of fractal dimensions related to different grain sizes. In this work, a single fixed value of fractal dimension related to grains larger than the smallest grain diameter was used to describe the PSD. The water retention and hydraulic conductivity functions for capillary water were derived based on this PSD through Young-Laplace's law and Mualem's model, whereas adsorption effects were accounted for based on the PID model. Our model confirms that, in fine grained soils, both capillary and adsorptive water affect the hydraulic properties at water content higher than residual, whereas solely the effect of adsorptive water remains at smaller water content.

The model is based on five physically based parameters: the air-entry value $h_{k,a}$, the residual water content θ_r, the fractal dimension of the grains D_f, the saturated film hydraulic conductivity K_s^{film}, and a parameter l accounting for the tortuosity and pore connectivity. The value of D_f can be computed based on the GSD, while $h_{k,a}$ and θ_r can be determined from water retention data. Finally, as in other models, solely K_s^{film} and l values need to be adjusted, based on hydraulic conductivity data.

The model has been tested on the published data sets of 14 different soils. The example of the Green Wave substrate confirms that good agreement with experimental data can be obtained when D_f is determined based on the GSD. For the 13 remaining soils, the GSD was not available, so D_f was adjusted based on water retention data. Smaller values of D_f appeared to be related to materials with more uniform GSD and PSD, such as sands, while higher D_f values were related to some clayey soils and well-graded granular materials with a nonnegligible percentage of clay particles. Higher values of θ_r are also related to materials with significant amount of fine particles. In this case, the adsorptive water has a more significant impact, especially on the water retention properties. In terms of the hydraulic conductivity, particularly in the low suction range, the contribution of adsorptive water is mostly negligible comparing to

capillary water, with lower values, by 1 to 5 orders of magnitude. In the case of the well-graded granular materials with 5% to 15% fines, the change in hydraulic conductivity with respect to suction is less significant, resulting in negative l values. It is thought that the strong physical basis of the model proposed here makes it convenient for water flow simulation through fine-grained soils along the full range of matric suctions.

Appendix A: Link Between the PSD and the GSD

In order to recognize from a ρ^{ind} field the cumulative distribution of grains with diameters equal to or larger than $d_g = L_1(\lambda)$, solely $\rho^{ind} \geq \rho^{ind}_{s,\,min}$ values at different λ are considered (see Stanić, 2020). Here, $\rho^{ind}_{s,\,min} = \dfrac{\rho_{s,\,min}}{\rho_{bulk}} > 1$ is a fixed threshold value equal to the ratio between the minimal grain density and the dry density of the material. By applying the upscaling technique, ρ^{ind} mitigates as λ decreases, causing also a progressive reduction of $P_{grains}(\lambda) = \dfrac{N_{grains}(\lambda)}{\lambda^E}$, where $N_{grains}(\lambda)$ is the number of $\rho^{ind} \geq \rho^{ind}_{s,\,min}$ values at different λ. As in case of the PSD function (Equation 4), which is obtained by renormalizing $P_{pores}(\lambda)$ with respect to $P_{pores}(\lambda_n)$, the GSD can be expressed in a similar way:

$$P\left(d < d_g\right) = 1 - \frac{P_{grains}(\lambda)}{P_{grains}(\lambda_n)}. \tag{A1}$$

Compared to the PSD, where $P_{pores}(\lambda) = 1 - P_{white}(\lambda)$ and $P_{white}(\lambda)$ is described analytically by means of the fractal law (Equation 1), $P_{grains}(\lambda)$ is described by means of the Universal Multifractals framework (see Stanić, 2020 for more details):

$$P_{grains}(\lambda) = \lambda^{-C_1\left(\frac{\ln\left(\rho^{ind}_{s,\,min}\right)}{\ln(\lambda)}\frac{1}{C_1\alpha'} + \frac{1}{\alpha}\right)^{\alpha'}}, \qquad \alpha' = \left(1 - \frac{1}{\alpha}\right)^{-1}, \quad \alpha \neq 1, \tag{A2}$$

where C_1 $[0 \div E]$ and α $[0 \div 2]$ are the mean intermittency and the multifractality index, respectively, both describing the heterogeneity of the investigated field. By introducing Equation A2 into A1, where $\lambda = L/d_g$, and by expressing $P_{grains}(\lambda_n)$ by means of Equation A2 as well, where $\lambda_n = L/d_{g,min}$, the multifractal-based GSD model is obtained:

$$P\left(d < d_g\right) = 1 - \frac{\left(\frac{L}{d_g}\right)^{-C_1\left(\frac{\ln\left(\rho^{ind}_{s,\,min}\right)}{\ln\left(L/d_g\right)}\frac{1}{C_1\alpha'} + \frac{1}{\alpha}\right)^{\alpha'}}}{\left(\frac{L}{d_{g,\,min}}\right)^{-C_1\left(\frac{\ln\left(\rho^{ind}_{s,\,min}\right)}{\ln\left(L/d_{g,\,min}\right)}\frac{1}{C_1\alpha'} + \frac{1}{\alpha}\right)^{\alpha'}}}. \tag{A3}$$

If all grains are recognized at λ_n, as mentioned in the main text, $P_{grains}(\lambda_n) = P_{white}(\lambda_n)$. Thus, D_f can be expressed by equalizing Equation 1 for $\lambda = \lambda_n$, where $\lambda_n = L/d_{g,min}$ and $\lambda_{min} = L/d_{p,max}$, with the term below the division sign in Equation A3:

$$D_f = 3 - C_1\left(\frac{\ln\left(\rho^{ind}_{s,\,min}\right)}{\ln\left(L/d_{g,\,min}\right)}\frac{1}{C_1\alpha'} + \frac{1}{\alpha}\right)^{\alpha'}\frac{\ln\left(\dfrac{L}{d_{g,\,min}}\right)}{\ln\left(\dfrac{d_{p,\,max}}{d_{g,\,min}}\right)}, \tag{A4}$$

where $d_{g,min} = d_{p,min} = L_1(\lambda_n)$. After determining the best fitting values of the GSD model parameters ($\rho^{ind}_{s,\,min}$, $d_{g,min}$, C_1 and α) and the value of $d_{p,max}$, the value of D_f is computed by means of Equation A4.

Data Availability Statement

Data archiving is underway, and authors are planning to use Zenodo repository. Temporarily, a copy of used data is uploaded as supporting information for review purposes.

Acknowledgments

The authors greatly acknowledge the Inter-laboratory PhD Merit Scholarship, provided by Ecole des Ponts ParisTech (Chair "Hydrology for resilient city") to the first author, which made this collaborative work possible.

References

Bird, N. R. A., Perrier, E., & Rieu, M. (2000). The water retention function for a model of soil structure with pore and solid fractal distributions. *European Journal of Soil Science*, *51*(1), 55–63. https://doi.org/10.1046/j.1365-2389.2000.00278.x

Brooks, R. H., & Corey, A. T. (1964). Hydraulic properties of porous media. *Hydrology Papers*, *3*, 1–27.

Burdine, N. T. (1953). Relative permeability calculations from pore size distribution data. *Journal of Petroleum Technology*, *5*(03), 71–78. https://doi.org/10.2118/225-g

Campbell, G. S., & Shiozawa, S. (1992). Prediction of hydraulic properties of soils using particle-size distribution and bulk density data. In *Proceedings of the international workshop on indirect methods for estimating the hydraulic properties of unsaturated soils* (pp. 317–328). Riverside: University of California.

Feder, J. (1988). *Fractals*. New York: Plenum Press.

Fredlund, D. G., & Xing, A. (1994). Equations for the soil-water characteristic curve. *Canadian Geotechnical Journal*, *31*, 521–532.

Ghanbarian-Alavijeh, B., Millán, H., & Huang, G. (2011). A review of fractal, prefractal and pore-solid-fractal models for parameterizing the soil water retention curve. *Canadian Journal of Soil Science*, *91*(1), 1–14. https://doi.org/10.4141/cjss10008

Hoffmann-Riem, H., van Genuchten, M. Th., & Flühler, H. (1997). A general model for the hydraulic conductivity of unsaturated soils. In *Proceedings of the international workshop on characterization and measurement of the hydraulic properties of unsaturated porous media* (pp. 31–42). Riverside: U.S. Department of Agriculture and University of California.

Iden, S. C., & Durner, W. (2014). Comment on 'Simple consistent models for water retention and hydraulic conductivity in the complete moisture Range' by A. Peters. *Water Resources Research*, *50*, 7530–7534. https://doi.org/10.1002/2014WR015937

Jackson, R. D., Reginato, R. J., & Van Bavel, C. H. M. (1965). Comparison of measured and calculated hydraulic conductivities of unsaturated soils. *Water Resources Research*, *1*(3), 375–380. https://doi.org/10.1029/wr001i003p00375

Jensen, D. K., Tuller, M., de Jonge, L. W., Arthur, E., & Moldrup, P. (2014). A new two-stage approach to predicting the soil water characteristic from saturation to oven-dryness. *Journal of Hydrology*, *521*, 498–507. https://doi.org/10.1016/j.jhydrol.2014.12.018

Kosugi, K. (1996). Lognormal distribution model for unsaturated soil hydraulic properties. *Water Resources Research*, *32*(9), 2697–2703.

Lenormand, R. (1990). Liquids in porous media. *Journal of Physics: Condensed Matter*, *2*, SA79–SA88.

Leong, E. C., & Rahardjo, H. (1997). Permeability Functions for Unsaturated Soils. *Journal of Geotechnical and Geoenvironmental Engineering*, *123*(12), 1118–1126.

Li, Y., & Wardlaw, N. C. (1986). Mechanisms of nonwetting phase trapping during imbibition at slow rates. *Journal of Colloid and Interface Science*, *109*(2), 473–486.

Likos, W. J., & Lu, N. (2003). Automated humidity system for measuring total suction characteristics of clay. *Geotechnical Testing Journal*, *26*(2). https://doi.org/10.1520/GTJ11321J

Lu, N. (2016). Generalized soil water retention equation for adsorption and capillarity. *Journal of Geotechnical and Geoenvironmental Engineering*, *142*(10), 04016051. https://doi.org/10.1061/(ASCE)GT.1943-5606.0001524

Lu, N., & Khorshidi, M. (2015). Mechanisms for soil-water retention and hysteresis at high suction range. *Journal of Geotechnical and Geoenvironmental Engineering*, *141*(8), 04015032. https://doi.org/10.1061/(ASCE)GT.1943-5606.0001325

Lu, N., & Zhang, C. (2019). Soil sorptive potential: Concept, theory, and verification. *Journal of Geotechnical and Geoenviromental Engineering*, *145*(4), 1–13. https://doi.org/10.1061/(ASCE)GT.1943-5606.0002025

Mehta, B. K., Shiozawa, S., & Nakano, M. (1994). Hydraulic properties of a sandy soil at low water contents. *Soil Science*, *157*(4), 208–214.

Mualem, Y. (1976). A new model for predicting the hydraulic conductivity of unsaturated porous media. *Water Resources Research*, *12*(3), 513–522. https://doi.org/10.1029/WR012i003p00513

Neto, D. D., van Lier, Q. J., van Genuchten, M. T., Reichardt, K., Metselaar, K., & Nielsen, D. R. (2011). Alternative analytical expressions for the general van Genuchten-Mualem and van Genuchten-Burdine hydraulic conductivity models. *Vadose Zone Journal*, *10*, 618–623. https://doi.org/10.2136/vzj2009.0191

Oh, S., Kim, Y. K., & Kim, J. -W. (2015). A modified van Genuchten-Mualem model of hydraulic conductivity in Korean residual soils. *Water*, *7*, 5487–5502. https://doi.org/10.3390/w7105487

Pachepsky, Y., Scherbakov, R., Varallyay, G., & Rajkai, K. (1984). On obtaining soil hydraulic conductivity curves from water retention curves [in Russian]. *Pochvovedenie*, *10*, 60–72.

Perrier, E., Bird, N., & Rieu, M. (1999). Generalizing the fractal model of soil structure: The pore-solid fractal approach. *Developments in Soil Science*, *27*(C), 47–74. https://doi.org/10.1016/S0166-2481(00)80005-7

Peters, A. (2013). Simple consistent models for water retention and hydraulic conductivity in the complete moisture range. *Water Resources Research*, *49*, 6765–6780. https://doi.org/10.1002/wrcr.20548

Peters, A., Durner, W., & Wessolek, G. (2011). Consistent parameter constraints for soil hydraulic functions. *Advances in Water Resources*, *34*(10), 1352–1365. https://doi.org/10.1016/j.advwatres.2011.07.006

Rudiyanto, S., van Genuchten, M. T., Alazba, A. A., Setiawan, B. I., & Minasny, B. (2015). A complete soil hydraulic model accounting for capillary and adsorptive water retention, capillary and film conductivity, and hysteresis. *Water Resources Research*, *51*, 1–16. https://doi.org/10.1002/2015WR017703

Russell, A. R., & Buzzi, O. (2012). A fractal basis for soil-water characteristics curves with hydraulic hysteresis. *Géotechnique*, *62*(3), 269–274. https://doi.org/10.1680/geot.10.P.119

Schaap, M. G., & Leij, F. J. (1999). Improved prediction of unsaturated hydraulic conductivity with the Mualem-van Genuchten model. *Soil Science Society of America Journal*, *64*, 843–851.

Stanić, F. (2020). High resolution monitoring and modelling of hydrological fluxes in a green roof (Doctoral dissertation). Université Paris-Est (Ecole des Ponts ParisTech), Paris, France.

Stanić, F., Cui, Y.-J., Delage, P., de Laure, E., Versini, P.-A., Schertzer, D., & Tchiguirinskaia, I. (2019). A device for the simultaneous determination of the water retention properties and the hydraulic conductivity function of an unsaturated coarse material; application to a green- roof volcanic substrate. *Geotechnical Testing Journal*, *43*(3), 20170443. https://doi.org/10.1520/GTJ20170443

Tokunaga, T. K. (2009). Hydraulic properties of adsorbed water films in unsaturated porous media. *Water Resources Research*, *45*, W06415. https://doi.org/10.1029/2009WR007734

Tuller, M., & Or, D. (2001). Hydraulic conductivity of variably saturated porous media: Film and corner flow in angular pore space. *Water Resources Research*, *37*(5), 1257–1276.

van Genuchten, M. T. (1980). A closed-form equation for predicting the hydraulic conductivity of unsaturated soils. *Soil Science Society of America Journal*, *44*(5), 892–898. https://doi.org/10.2136/sssaj1980.%0A03615995004400050002x

Wang, Y., Ma, J., & Guan, H. (2016). A mathematically continuous model for describing the hydraulic properties of unsaturated porous media over the entire range of matric suctions. *Journal of Hydrology*, *541*, 873–888. https://doi.org/10.1016/j.jhydrol.2016.07.046

Wang, Y., Ma, J., Zhang, Y., Zhao, M., & Edmunds, W. M. (2013). A new theoretical model accounting for film flow in unsaturated porous media. *Water Resources Research*, *49*, 5021–5028. https://doi.org/10.1002/wrcr.20390

Xu, Y. (2004). Calculation of unsaturated hydraulic conductivity using a fractal model for the pore-size distribution. *Computers and Geotechnics*, *31*, 549–557. https://doi.org/10.1016/j.compgeo.2004.07.003

Yang, H., Khoshghalb, A., & Russell, A. R. (2014). Fractal-based estimation of hydraulic conductivity from soil—Water characteristic curves considering hysteresis. *Géotechnique Letters*, *4*, 1–10. https://doi.org/10.1680/geolett.13.00071

Yates, S. R., Warrick, A. W., & Leij, F. J. (1991). Analysis of measured, predicted, and estimated hydraulic conductivity using the RETC computer program. *Soil Science Society of America Journal*, *56*, 347–354.

Yu, B., & Cheng, P. (2002). A fractal permeability model for bi-dispersed porous media. *International Journal of Heat and Mass Transfer*, *45*, 2983–2993.

Zhang, C., & Lu, N. (2019). Unitary definition of matric suction. *Journal of Geotechnical and Geoenviromental Engineering*, *145*(2). https://doi.org/10.1061/(ASCE)GT.1943-5606.0002004

Zhang, C., & Lu, N. (2020). Soil Sorptive potential: Its determination and predicting soil water density. *Journal of Geotechnical and Geoenviromental Engineering*, *146*(1), 1–10. https://doi.org/10.1061/(ASCE)GT.1943-5606.0002188

Zhang, Z. F. (2011). Soil water retention and relative permeability for conditions from oven-dry to full saturation. *Vadose Zone Journal*, *10*, 1299–1308. https://doi.org/10.2136/vzj2011.0019